PAPER • OPEN ACCESS

Effect of 4.6 GHz LHW on tungsten transport in NBI dominant H-mode plasma in EAST tokamak

To cite this article: Yunxin Cheng *et al* 2025 *Nucl. Fusion* **65** 062003

View the article online for updates and enhancements.

Effect of 4.6 GHz LHW on tungsten transport in NBI dominant H-mode plasma in EAST tokamak

Yunxin Cheng[1] [iD], Ling Zhang[1,*], Chengxi Zhou[1,*] [iD], Shigeru Morita[1,2], Xiang Gao[1] [iD], Shouxin Wang[1] [iD], Ailan Hu[1], Wenmin Zhang[1,3] [iD], Zhen Zhou[1] [iD], Qing Zang[1], Jianwen Liu[1], Fang Ding[1], Yanmin Duan[1], Liqing Xu[1] [iD], Yingying Li[4] [iD], Mao Wang[1], Miaohui Li[1] [iD], Jihui Chen[1], Darío Mitnik[5] [iD], Jinping Qian[1], Haiqing Liu[1] [iD], Guosheng Xu[1] [iD], Jiansheng Hu[1] and Yuntao Song[1]

[1] Institute of Plasma Physics Chinese Academy of Sciences, Hefei 230031, China
[2] National Institute for Fusion Science, Toki, 509-5292 Gifu, Japan
[3] Science Island Branch of Graduate School, University of Science and Technology of China, Hefei 230031, China
[4] Hebei Key Laboratory of Compact Fusion, Langfang 065001, China
[5] Instituto de Astronomía y Física del Espacio (CONICET-Universidad de Buenos Aires), Buenos Aires 1428, Argentina

E-mail: zhangling@ipp.ac.cn and chengxi.zhou@ipp.ac.cn

CrossMark

Abstract

Experimental observations in EAST tokamak have revealed a notable suppression of tungsten accumulation during the lower hybrid wave (LHW) injection in the neutral beam injection (NBI)-heated H-mode plasma. The variation in tungsten concentration during the LHW phase is quantified using the intensity of tungsten unresolved transition array (W-UTA), as measured by the extreme ultraviolet spectrometer. After the LHW is turned on, the tungsten concentration, $C_W = n_W/n_e$, decreased by approximately 45%, from 9.5×10^{-5} to 5.3×10^{-5}. Additionally, the peaked tungsten profile is flattened, with the peak position shifted outward, implying a significant alteration in tungsten transport. The observed results suggest that reduced toroidal rotation and increased electron temperature are responsible for the variation in tungsten transport during the LHW heating. Modeling using a simulation code of Transport in Gyrokinetic Plasmas with Rotation and Optimization (TGYRO) indicates that, after the LHW injection, the turbulent diffusion of tungsten ions is enhanced and the neoclassical convection is weakened. Moreover, comparisons of the transport coefficients of tungsten ions under different plasma parameters reveal that the LHW heating enhances the turbulent diffusion of tungsten ions by increasing the electron temperature gradient. It also decreases the plasma toroidal rotation velocity, which in turn reduces the inward neoclassical convection of tungsten ions. These

---

* Authors to whom any correspondence should be addressed.

findings provide a feasible solution for the tungsten accumulation induced by the NBI heating, supporting EAST in achieving long-pulse high-performance plasma discharge. This work offers an important reference for the operation of ITER and the design of future fusion reactors.

(Some figures may appear in colour only in the online journal)

1. Introduction

In magnetic confinement fusion research, tungsten is considered as a potential candidate material for plasma-facing components (PFC) in ITER [1] and future reactors, like CFETR [2], due to its excellent characteristics of high sputtering threshold and high neutron resistance. However, as a high-Z element, tungsten ions do not fully ionize within the temperature range of fusion plasmas, leading to substantial radiation power loss and increased potential for plasma collapse. During the collapse, a significant damage to the tokamak wall is caused by heat deposition, electromagnetic stress, runaway electrons and so on. Therefore, controlling the tungsten atom/ions in the plasma is a critical challenge for fusion research.

Tungsten accumulation often occurs in neutral beam injection (NBI)-dominated H-mode plasma because the NBI accelerates the toroidal rotation of the plasma, leading to an asymmetric distribution of tungsten density and enhancing the inward neoclassical convection [3, 4]. Moreover, the particle source directly brought by the NBI increases the density gradient, further enhancing the inward neoclassical convection and exacerbating the accumulation of tungsten ions in the plasma [5, 6]. Studies in ASDEX-U tokamak have suggested that on-axis electron cyclotron resonance heating (ECRH) can be used to control the tungsten accumulation by increasing the electron temperature [7]. A high electron temperature gradient (ETG) plays a key role in generating a large turbulent diffusion [7, 8]. In JET tokamak, it has been found that on-axis ion cyclotron resonance heating (ICRH) with sufficient power can reduce the ratio of density gradient to ion temperature gradient (ITG) and increase the neoclassical outward convection, thereby significantly suppressing the tungsten accumulation [5, 9]. However, the RF-sheath near the ICRH antenna introduces additional impurity sources, leading to a significant increase in the impurity content in the plasma [10, 11].

In EAST, lower hybrid wave (LHW) has been demonstrated to exhibit a significant effect of plasma current drive, playing an indispensable role in achieving a super long-pulse discharge, such as 403 s H-mode and 1056 s I-mode steady-state discharges [12, 13]. In discharges with relatively high-power NBI, however, the long-pulse H-mode operation has been often restricted by the tungsten accumulation. Recently, a reproducible long-pulse H-mode operation with sufficient tungsten suppression has been successfully achieved in the LHW-heated discharge, and then various experimental approaches have been explored to mitigate the tungsten accumulation [14–16]. Experimental studies in EAST also indicate that the tungsten accumulation can be suppressed in

the NBI discharge when the 4.6 GHz LHW is superimposed. Furthermore, the tungsten concentration is reduced by an order of magnitude when the ratio of LHW power to total injection power, $P_{LHW}/(P_{LHW} + P_{NBI})$, exceeds 0.8.

Currently, studies of the impact of LHW on tungsten impurity transport and the role on the tungsten impurity content control remain limited. Recent findings in EAST suggest that the LHW can influence the tungsten transport and suppress the tungsten accumulation effectively in the NBI-dominant H-mode discharge. In this work, therefore, experimental observations and simulation analyses are combined to investigate how the LHW affects tungsten impurity transport. The structure of this paper is as follows. The diagnostics in EAST and the simulation codes for data analyses are introduced in section 2. Section 3 presents results of the experimental observation on tungsten impurity behavior in low- and high-q_{95} plasmas. Results of the tungsten transport analyses based on the TYGRO and STRAHL codes are described in section 4. Discussions and conclusions are given in sections 5 and 6, respectively.

2. Experimental setup

EAST ($R/a = 1.85$ m/0.45 m, $I_p = 1$ MA and $B_t = 2.0$–3.5 T) is a full superconducting tokamak with flexible divertor configurations, i.e. lower single null, double null and upper single null configurations. In 2014 and 2021, the original graphite upper and lower divertors were replaced by tungsten materials, respectively, to enhance the divertor heat load capability during the long-pulse high-performance plasma discharge [17]. To minimize the 'hot spot' effect, graphite guard limiters of the LHW antenna were also replaced by tungsten materials in 2018 [18]. In 2022, the main limiter was upgraded to tungsten materials to further validate the feasibility of ITER operation scenario [19]. Consequently, the EAST tokamak continued to operate the discharge under full tungsten divertor and limiter environments to this day, despite frequent tungsten bursts induced. Recently, several heating systems have been upgraded in EAST. It enables to explore multiple heating schemes on the study of H-mode discharges. The heating systems applied in this work include co-injection NBIs [20], ECRH [21] and LHW [22]. The LHW frequency of 4.6 GHz is utilized with a parallel refractive index of $n_{//} = 2.04$ and a phase difference of 90° between adjacent main waveguides to achieve the optimal coupling efficiency.

To study the tungsten behavior in EAST H-mode discharges, two fast-time-response extreme ultraviolet (EUV) spectrometers with a time evolution of 5 ms have been
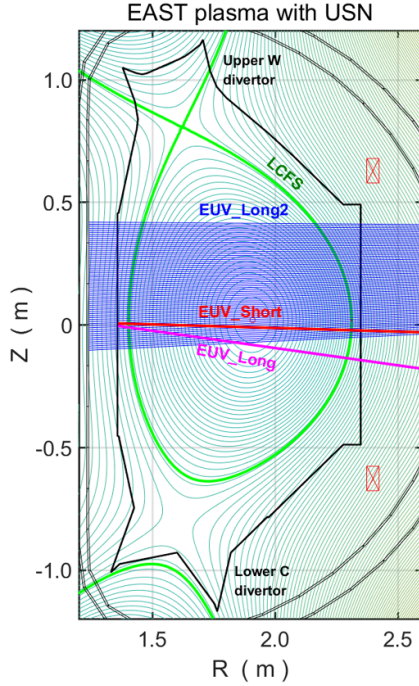
Figure 1. Observation chords of fast-time-response EUV spectrometers (EUV_Long and EUV_Short) and space-resolve EUV spectrometer (EUV_Long2). The data used in this study was taken before 2020, when carbon materials were used on the lower divertor.

developed in EAST, named 'EUV_Short' and 'EUV_Long', working in the wavelength ranges of 5–138 Å [23] and 20–520 Å [24], respectively. A space-resolved EUV spectrometer, named 'EUV_Long2', working in 20–520 Å has been used to measure the radial profile of line emissions from highly ionized tungsten ions in EAST [25]. A charge-coupled detector (CCD) is used for the spectrometers. The observation range of the space-resolved EUV spectrometer is $-10 \leqslant Z \leqslant 40$ cm at $R = 1.9$ m. Figure 1 shows the line of sight of the EUV spectrometers in EAST plasma. In general, the impurity species may be distinguished by three categories as low-Z impurities ($Z \leqslant 18$), medium-Z impurities ($18 < Z < 32$) and high-Z impurities ($Z \geqslant 32$), depending on the difference in the ionization energy. For simplicity, in this study, the impurity species are distinguished by two categories of low-Z ($Z \leqslant 18$) and high-Z ($Z > 18$) impurities because the electron temperature of EAST plasma is near the ionization energy of helium-like ($E_i = 4121$ eV) and hydrogen-like ($E_i = 4426$ eV) argon ions. Based on the EUV spectrometers, the line emissions from intrinsic low-Z (He, Li, C, N and O) and high-Z (Fe, Cu, Mo and W) impurity ions with different ionization stages have been observed and identified in the EAST plasma [26–28]. The tungsten concentration, C_w ($=n_W/n_e$), is evaluated with a combination of the intensity of tungsten unresolved transition array (W-UTA) in 45–70 Å and cooling factor. Moreover, the density profile of Fe^{22+}, Mo^{31+}-Mo^{32+} and W^{43+}-W^{45+} ions can be calculated utilizing Abel inversion and photon emission coefficients from ADAS database [29].

In the experiment radial profiles of the electron temperature, T_e, are provided by Thomson scattering

diagnostic [30] and 16-channel heterodyne radiometer [31], and radial profiles of electron density, n_e, are measured by polarimeter-interferometer [32] and microwave reflectometry [33]. A tungsten source from upper divertor is evaluated from the line intensity of W I at 4009 Å measured by divertor visible spectroscopy [34]. Total radiation power loss is evaluated from a resistive bolometer system [35]. In the framework of the theory-based modeling carried out in this paper, radial profiles of the tungsten transport coefficients are simulated by Transport in Gyrokinetic Plasmas with Rotation and Optimization (TGYRO) [36] which is linked to a drift-kinetic code, NEO [37, 38], and a trapped gyro-Landau-fluid code, TGLF [39–41], to calculate the neoclassical and turbulent transports. The density profiles of tungsten and other impurity ions are simulated by an impurity transport code, STRAHL [42], along with the emission rates of all charge states of the impurity ions, based on the provided transport coefficients.

3. Tungsten suppression with LHW injection

In recent EAST experiments, lithium coating [43] and real-time lithium powder injection [44] have been carried out to suppress the tungsten source, in particular, in H-mode discharges. However, the tungsten ion still exists in the core plasma with a considerably high concentration. To control the tungsten accumulation in the NBI-heated H-mode discharge, experiments have been performed by superimposing the LHW heating. Initial results on the tungsten accumulation suppression are obtained in the H-mode discharge [16]. For more comprehensive understandings on the combined heating effect of LHW and NBI and further better control of the tungsten accumulation, several heating combinations have been explored in EAST. The low and high q_{95} plasmas represent two typical discharge parameter regimes in the EAST tokamak. In both regimes the suppression of tungsten impurity ions accumulation by the additional LHW heating has been observed.

3.1. Experimental observations of tungsten impurity behavior in low q_{95} plasma

Time traces of the NBI-dominant H-mode discharge with upper single null divertor configuration (shot #80672) under a low toroidal magnetic field ($B_T = 1.67$ T) are shown in figure 2. The 4.6 GHz LHW with $P_{LHW} = 1.5$ MW is injected during the steady phase with $P_{NBI} = 2.0$ MW. The 0.7 MW 2.45 GHz LHW is kept almost constant to drive the plasma current. The plasma current, central electron temperature and line-averaged electron density are 450 kA, 2.0 keV and 3.0×10^{19} m^{-3}, respectively, with q_{95} of 4.0. After the first NBI injection the plasma moves to ELMy H-mode phase at $t = 3.15$ s. The second NBI injection started at $t = 3.3$ s leads to further increase in toroidal rotation velocity and tungsten concentration. The H–L transition is triggered at $t = 7.3$ s after the NBI is turned off. When the LHW is switched on, the ELM frequency (f_{ELM}) increases from 70 Hz to 100 Hz, and decreases to 75 Hz after the LHW is turned off, as shown in figure 2(*c*). Although the increase in f_{ELM} could flush out the tungsten ion, the amplitude of D_α signal slightly increases during the
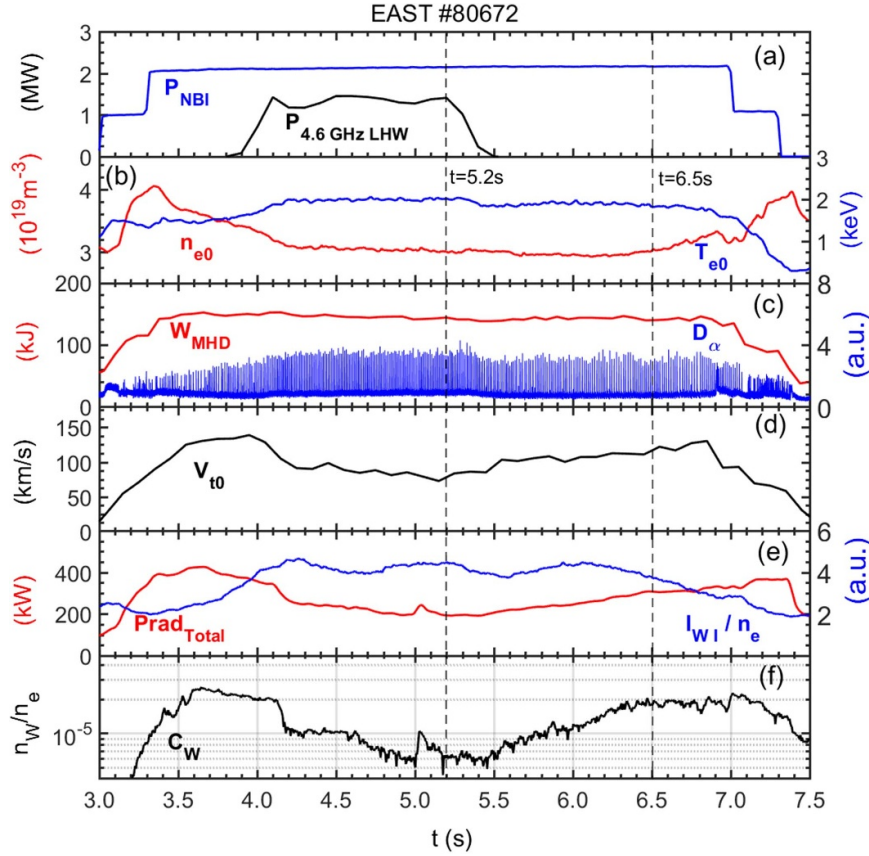
Figure 2. Time evolution of (*a*) P_{NBI}, $P_{4.6GHz\,LHW}$, (*b*) line-averaged electron density, n_{e0}, and central electron temperature, T_{e0}, (*c*) plasma stored energy, W_{MHD}, and D_α intensity of upper divertor, (*d*) central toroidal rotation velocity, V_{t0}, (*e*) total radiation power loss, $P_{rad\,total}$, and W I (4009 Å) line emission, (*f*) tungsten concentration in plasma core in #80672 discharge. Time slices of $t = 5.2$ s and $t = 6.5$ s denoted with vertical dashed lines are selected for data analyses on EUV spectra and radial profiles.

LHW injection, indicating an enhancement of the plasma wall interaction (PWI), which in turn also enhances the tungsten source. The tungsten source, as seen in the W I line emission in figure 2(*e*), continuously increases due to the enhancement of PWI during the LHW phase. Despite this, the tungsten concentration in the plasma core decreases from 2.0×10^{-5} to 6×10^{-6} during the LHW injection and radiation power loss also significantly reduces from 350 kW to 200 kW, as shown in figures 2(*e*) and (*f*), respectively. The significant decrease in the tungsten concentration and radiation power is associated with a reduction in the toroidal rotation velocity, which decreases from 130 km s^{-1} to 70 km s^{-1} during the LHW heating as shown in figure 2(*d*). After the LHW is switched off, the toroidal rotation velocity, tungsten concentration and radiation power continue to rise, reaching $V_t = 110$ km s^{-1}, $C_W = 1.8 \times 10^{-5}$ and $P_{rad} = 300$ kW, respectively, at $t = 6.5$ s. Notably, the spontaneous decrease in the tungsten concentration during $t = 3.5–4.1$ s may be related to the fishbone mode instability triggered by high-energy particles, as shown in figure 3. The fishbone mode stabilized during the LHW phase can control the impurity accumulation [45], and its effect on the impurity ions is similar to that of sawtooth instability [46].

Figure 4 presents EUV spectra observed with and without LHW injection in shot #80672. The line emissions from low-Z impurity ions, such as CVI 33.734 Å, N VII 24.78 Å, O VII 21.602 Å and O VIII 18.97 Å are identified in the short wavelength range of 10–40 Å. The W-UTA in the wavelength range of 45–70 Å is composed of line emissions from low-ionized tungsten ions, e.g. W^{26+}-W^{32+}, due to the low electron temperature of 2 keV in this discharge. In the wavelength range of 70–195 Å, several isolated line emissions from metallic impurity ions are identified, e.g. Mo XXXII 127.868 Å, Fe XXIII 132.906 Å and Cu XXIV 111.186 Å. During the LHW phase, the intensity of line emissions from low-Z impurity ions (Li, C, N, O and Ne) is obviously unchanged, whereas the intensity of line emissions from high-Z impurity ions (Fe, Cu, Mo and W) substantially decreases. The intensity reduction of high-Z impurity line emissions suggests an effective control of the impurity accumulation during LHW heating.

Figure 5 illustrates the time evolution of the intensity normalized by n_e, I/n_e, for low- and high-Z impurity ions in the plasma core. During the 4.6 GHz LHW injection, the content of low-Z impurity was unchanged obviously, while the intensity of Li^{2+} ions slightly increased due to an enhanced
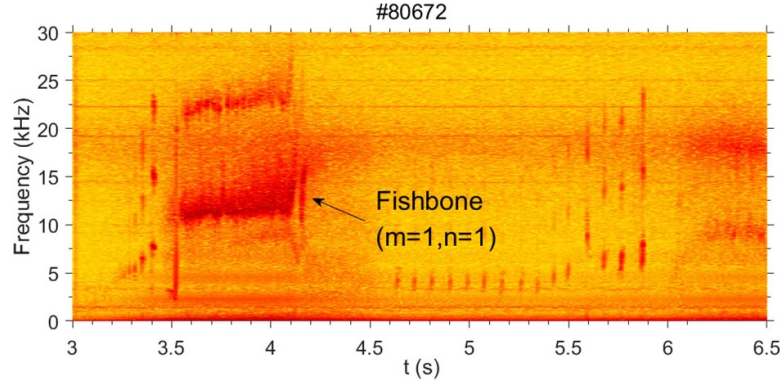
Figure 3. Frequency spectra at central chord of soft x-ray emission signals.
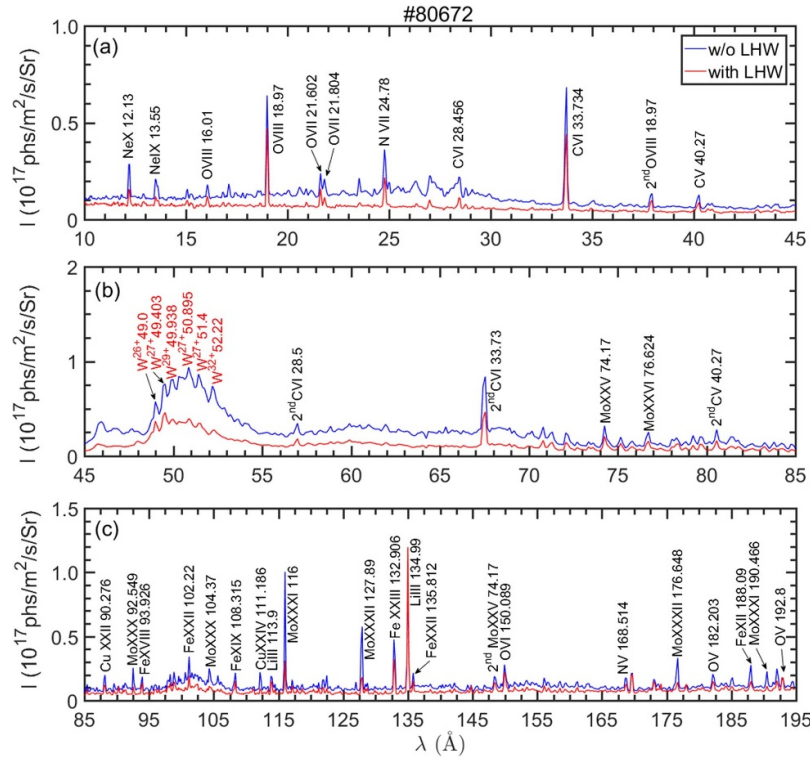

Figure 4. EUV spectra in wavelength ranges of (*a*) 10–45 Å, (*b*) 45–85 Å and (*c*) 85–195 Å observed with fast-time-response EUV spectrometers during H-mode phase with (at $t = 5.2$ s) and without (at $t = 6.5$ s) 4.6 GHz LHW in #80672 discharge of which the central electron temperature is 2 keV.

plasma-wall interaction, as shown in figures 5(*a*)–(*d*). In contrast, the content of high-*Z* metallic impurity ions significantly decreased during the LHW injection, but began to increase again after switching off the LHW, as presented in figures 5(*e*) and (*f*). The ratio of I/n_e after ($t = 6.5$ s) and during ($t = 5.2$ s) the LHW is listed in table 1 for metallic impurity ions. Due to formation of the peaked radial profile of the electron temperature, metallic impurity ions in high ionization stages like Fe^{22+} and Mo^{30+} ions are more localized in the plasma core. During the LHW phase, then, the change in the density of such highly ionized ions is bigger than that of low-ionized impurity ions staying in the plasma edge. It suggests that the LHW effect on impurity transport is more pronounced for impurity ions staying in the plasma core than those in the plasma edge.

For instance, after turning off the LHW, the I/n_e of W^{32+} ions increases by 256.5%, while the I/n_e of W^{29+} and W^{27+} ions in relatively lower ionization stages shows smaller increase of 206.1% and 132.4%, respectively. A similar trend also appears in behaviors of Mo and Fe ions. The W-UTA is composed of line emission from W^{26+}-W^{32+} ions with ionization energies ranging from 0.881 keV to 1.335 keV. The ionization energy of Mo^{30+} and Mo^{31+} ions are 1.730 keV and 1.790 keV, respectively. Despite the lower ionization energy of tungsten ions (W^{27+}, W^{29+} and W^{32+}) and molybdenum ions (Mo^{24+}, Mo^{30+} and Mo^{31+}), changes in the content of Mo ($Z = 42$) and W ($Z = 74$) ions during the LHW phase are more substantial compared to Fe ($Z = 26$) ions. The relative content of low-*Z* impurity ions (C^{4+}, C^{5+}, N^{6+}, O^{6+} and O^{7+}) in the plasma
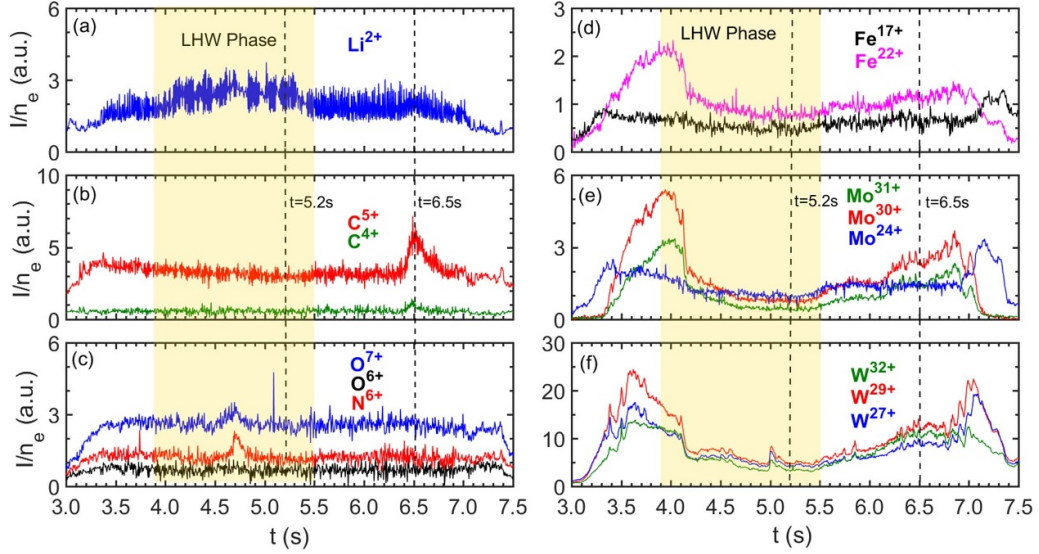
Figure 5. Time evolution of n_e-normalized line intensity of (*a*) Li^{2+} 135 Å, (*b*) C^{4+} 40.27 Å and C^{5+} 33.73 Å, (*c*) N^{6+} 24.78 Å, O^{7+} 18.97 Å and O^{6+} 21.6 Å, (*d*) Fe^{22+} 132.91 Å and Fe^{17+} 93.926 Å, (*e*) Mo^{31+}127.868 Å, Mo^{30+} 116 Å and Mo^{24+} 74.17 Å, (*f*) W^{32+} 52.22 Å, W^{29+} 49.938 Å and W^{27+} 49.403 Å observed with fast-time-response EUV spectrometers in # 80672 discharge. Timing of 4.6GHz LHW injection is denoted with shaded area and two vertical dashed lines indicate timings at which the ratio is calculated in table 1.

Table 1. Line emissions from metallic ions used in the present study (#80672 discharge).

Ions	Lines	E_i (eV)[a]	λ(Å)[b]	Ratios after and during LHW[c]
Fe^{17+}	Fe XVIII	1357.8	93.926	11.0%
Fe^{22+}	Fe XXIII	1950.4	132.91	38.7%
Mo^{24+}	Mo XXV	1263.0	74.17	116.9%
Mo^{30+}	Mo XXXI	1730.1	116.0	247.5%
Mo^{31+}	Mo XXXII	1790.9	127.868	330.8%
W^{27+}	W XXVIII	881.4	49.403	132.4%
W^{29+}	W XXX	1180.0	49.938	206.1%
W^{32+}	W XXXIII	1335.1	52.22	256.5%

[a] E_i: ionization energies of ions.
[b] λ: wavelengths of lines.
[c] n_e-normalized line intensity ratios after and during LHW taken at $t = 6.5$ s and $t = 5.2$ s, respectively.

edge exhibited no significant change during the LHW phase, with the exception of Li^{2+} ions which shows a slight increase during the LHW heating. The time behavior of the impurity ions suggests that the LHW may significantly influence impurity transport itself. This influence is likely related to the atomic number of impurity ions, particularly through neoclassical transport [42].

The LHW heating has a significant impact on the tungsten radial profile. The radial intensity profile of line emissions from W^{27+} and W^{32+} ions is observed by the space-resolved EUV spectrometer system at $t = 5.2$ s (during LHW) and $t = 6.5$ s (after LHW). Results are plotted in figure 6. During the LHW phase, the radial profile of W^{27+} and W^{32+} ions is flattened. In the radial region at $\rho < 0.3$, the tungsten ion content is significantly reduced. After the LHW is turned off, both W^{32+} and W^{27+} ions begin to accumulate in the plasma core. This significant change in the tungsten radial profile suggests that the LHW has a substantial impact

on tungsten impurity transport. The electron temperature profile remains unchanged after turning off the LHW, showing only a slight reduction in the plasma core, i.e. 2.0–1.8 keV, as plotted in figure 7(*a*). Due to a fringe jump in the signal of the polarimeter-interferometer system [32] after $t = 5.8$ s, no electron density profile is measured at $t = 6.5$ s (see figure 7(*b*)). However, according to the line-averaged density measured by hydrogen cyanide interferometer [47], as illustrated in figure 2(*b*), the electron density appears to remain unchanged after the LHW is turned off. Notably, during the LHW phase, the central ion temperature reduces from 1.6 keV to 1.3 keV (see figure 7(*c*)), and the central toroidal rotation velocity also reduces markedly (see figure 7(*d*). The toroidal rotation can be enhanced by the neoclassical inward pinch of high-*Z* impurity ions. Therefore, the reduction of the toroidal rotation velocity is one of the primary reasons why the high-*Z* metallic impurity ion content decreases during the LHW.
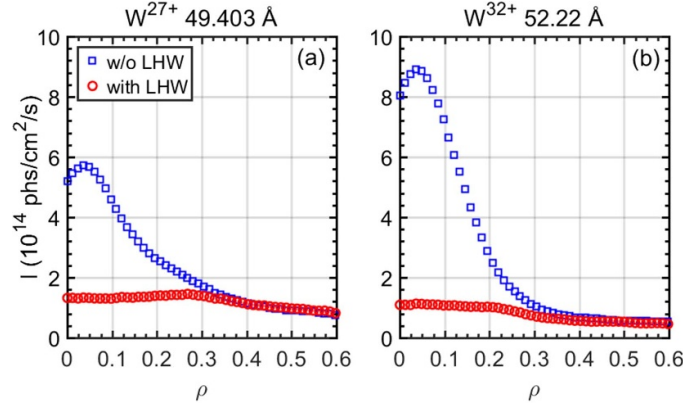
Figure 6. Vertical intensity profiles of (*a*) W^{27+} at 49.403 Å and (*b*) W^{32+} at 52.22 Å observed in #80672 discharge. Data of red circles and blue squares are measured at $t = 5.2$ s (with LHW) and $t = 6.5$ s (without LHW), respectively.
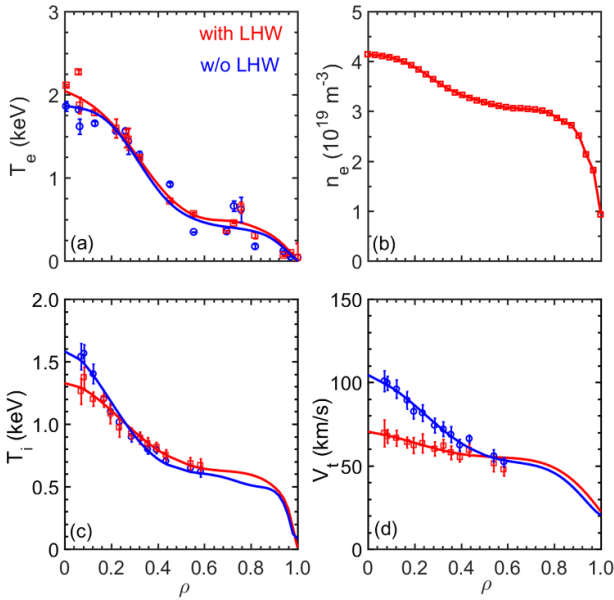

Figure 7. Radial profiles of (*a*) electron temperature from Thomson scattering system [30], (*b*) electron density from polarimeter-interferometer [32], (*c*) ion temperature and (*d*) toroidal rotation from charge exchange recombination spectroscopy [48]. Data of red squares and blue circles are observed at $t = 5.2$ s (with LHW) and $t = 6.5$ s (without LHW) in #80672 discharge, respectively. Solid lines indicate fitting curves based on measured experimental data.

3.2. Experimental observation of tungsten impurity behaviors in high q_{95} plasma

A high q_{95} ($q_{95} = 6.0$) discharge with upper single null configuration ($B_t = 2.55$ T and $I_p = 500$ kA) is conducted with intermittently injected 4.6 GHz LHW during NBI H-mode phase. The temporal evolution of plasma parameters and impurity content in the discharge is illustrated in figure 8. The LHW with $P_{LHW} = 1.5$ MW is injected at a frequency of 3 Hz and a duty cycle of 50% during the steady discharge phase with $P_{NBI} = 2.0$ MW. Low-power ECRH with $P_{ECRH} = 0.3$ MW is also injected throughout the discharge period to maintain a high electron temperature of 3.3 keV. Before switching on the

LHW, a clear improvement on the particle confinement after the L–H transition is evident in the temporal density behavior at $t = 2.6$ s. The tungsten content continues to increase from $t = 2.6$ s to $t = 3.2$ s, as shown in figures 8(*f*) and (*h*). This increase is likely due to the enhanced particle confinement and the consequent accumulation of impurity ions in the plasma core.

The intensity of the central channel signal of the electron cyclotron emission (ECE) [31] increases with the LHW injection, indicating effective electron heating by the LHW. Simultaneously, the ELM frequency, f_{ELM}, starts to increase and reaches 180 Hz, while it decreases to 120 Hz after switching off the LHW, as evidenced by the D_α signal in figure 8(*c*). During the LHW, the tungsten source estimated from W I line emission increases by 50%–80% (see figure 8(*d*)). Similar to the shot #80672, the tungsten concentration (C_w) significantly decreases during the LHW, despite the enhancement of the tungsten source. The C_W is approximately 9.5×10^{-5} in the discharge phase without LHW. However, the C_w reduces by about 45%, i.e. 5.3×10^{-5}. Further interest lies in the temporal behavior of line emissions from W^{26+}-W^{29+} and W^{43+}-W^{45+} ions, as shown in figure 8(*f*). The reduction ratio of tungsten impurity ions during the LHW exhibits different variations among charge states. The content of W^{43+}-W^{45+} ions predominantly locating near the plasma core decreases by 55%, whereas the content of W^{26+}-W^{29+} ions distributing near the plasma edge reduces by 40%. A similar drastic change is observed in the total radiation power loss, as shown in figure 8(*g*). The total radiation power loss, along with the tungsten impurity content, continues to increase during the NBI phase before $t = 3.5$ s. This intermittent increase and decrease in the tungsten concentration are related to changes in the toroidal rotation velocity and electron temperature induced by the LHW. Figure 8(*e*) clearly illustrates the relationship between the LHW and toroidal rotation velocity. During the LHW phase, the toroidal rotation velocity decreases to approximately 75 km s^{-1}, while it progressively increases to more than 100 km s^{-1} during the NBI phase without LHW pulse.

Owing to the higher central electron temperature of 3.0 keV, several line emissions from highly ionized tungsten ions are observed through the EUV spectrometers, e.g. W^{38+}
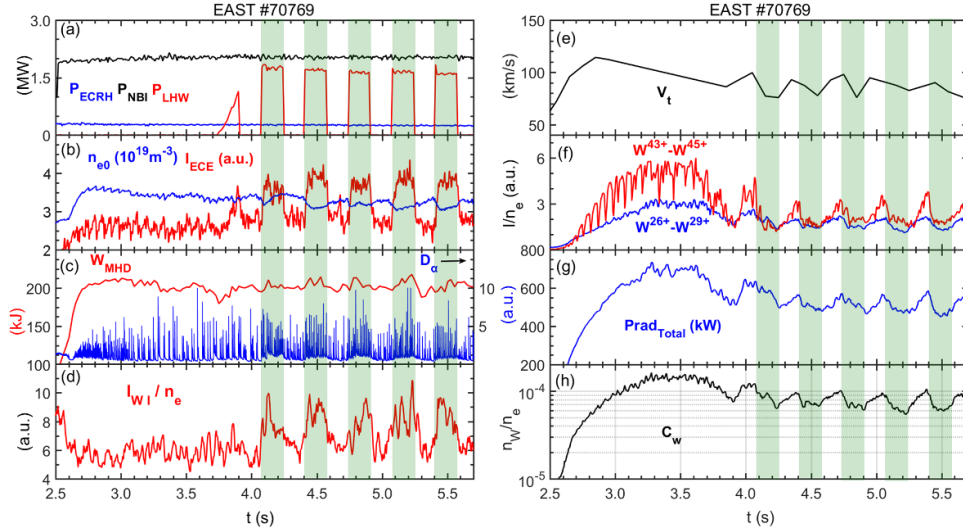
Figure 8. Time evolution of (*a*) heating power, P_{NBI}, P_{ECRH} and P_{LHW}, (*b*) line-averaged electron density, n_{e0}, and intensity of central ECE signal, I_{ECE}, (*c*) plasma stored energy, W_{MHD}, and D_α intensity at upper divertor, (*d*) intensity of W I (4009 Å) line emission, (*e*) central toroidal rotation velocity, V_{t0}, (*f*) W^{43+}-W^{45+} intensity at plasma core and W^{26+}-W^{29+} intensity at plasma outer region, (*g*) total radiation power loss, $Prad_{Total}$, and (*h*) tungsten concentration, C_W in #70769 discharge. Timings of intermittent LHW injection are denoted with green shaded area.

at 63.883 Å, W^{40+} at 65.873 Å, W^{41+} at 131.21 Å, W^{43+} at 61.334 Å and 126.29 Å, W^{44+} at 60.93 Å, and W^{45+} at 62.336 Å and 126.998 Å, as shown in figure 9. Some spectral lines unfortunately overlap due to their closely proximate wavelengths, e.g. W^{41+} at 47.048 Å and W^{42+} at 47.191 Å, and W^{44+} at 132.88 Å and Fe XXIII 132.91 Å. These tungsten lines are crucial for studying tungsten impurity transport. The line emission intensity of tungsten ions is significantly reduced with the LHW injection. It becomes remarkable in the case of highly ionized tungsten ions. In contrast, the line intensity of low-*Z* impurity ions remains unchanged during LHW.

Figure 10 illustrates radial intensity profiles of line emissions from W^{27+}, W^{32+}, W^{38+}, W^{41+} (W^{42+}), W^{43+} and W^{45+} ions observed during the NBI and LHW superimposed phase by the space-resolved EUV spectrometer. Since the sampling time of the CCD detector was set to 800 ms/frame in this discharge to enhance the signal-to-noise ratio, temporal behavior of the tungsten radial profile during the LHW pulse could not be studied. Therefore, the radial profiles plotted in figure 10 are the signal accumulated from $t = 3.3$ s to $t = 4.1$ s and $t = 4.9$ s to $t = 5.7$ s. Nevertheless, the observed result indicates a pronounced alteration in the tungsten radial profile from NBI to LHW phases. It is found that the radial intensity profiles of W^{41+}, W^{42+}, W^{43+} and W^{45+} ions are strongly peaked during the NBI phase. However, these profiles are flattened during the LHW phase with extremely low intensities. The line intensity profile of W^{27+} and W^{32+} ions located in outer plasma region are also flattened during the LHW phase. Furthermore, the peak position of the W^{27+}, W^{32+} and W^{38+} profiles shifts outwardly and the intensity gradient of the W^{41+}, W^{42+}, W^{43+} and W^{45+} profiles becomes moderate during the LHW phase. The drastic variation in the tungsten

intensity profile implies that the LHW has a significant influence to the tungsten transport process, and it may be associated with the toroidal rotation and electron temperature. Radial profiles of T_e, n_e, T_i and V_t are shown in figure 11. The data are taken at $t = 4.80$ s during the LHW pulse and at $t = 5.0$ s between two LHW pulses in the #70769 discharge. As the n_e profile does not change so much between two cases with and without LHW, the significant variation in the tungsten content does not originate from changes in the electron density profile. However, both ion temperature and toroidal rotation velocity noticeably decrease after the LHW pulse, as illustrated in figures 11(*c*) and (*d*). The electron temperature increases during the LHW, in particular, the central electron temperature increases from 2.6 keV to 3.3 keV. The variations in these parameter profiles are primarily responsible for the alteration of tungsten transport induced by the LHW.

4. Simulation results

Based on the plasma parameter profiles from shot #70769, as shown in figure 11, the TGYRO code is utilized to calculate the radial profile of tungsten transport coefficients under varying conditions. To estimate the transport coefficients, TGYRO utilizes experimentally measured profiles, such as electron temperature, ion temperature, electron density and toroidal rotation as initial input profiles. Through the iterative coupling with gyrokinetic simulations, TGYRO calculates and updates the transport coefficients until the simulated profiles converge to the experimental profiles. More detailed descriptions and specific settings on the TGYRO code can be found in the following [49]. Effects of the LHW heating, toroidal rotation
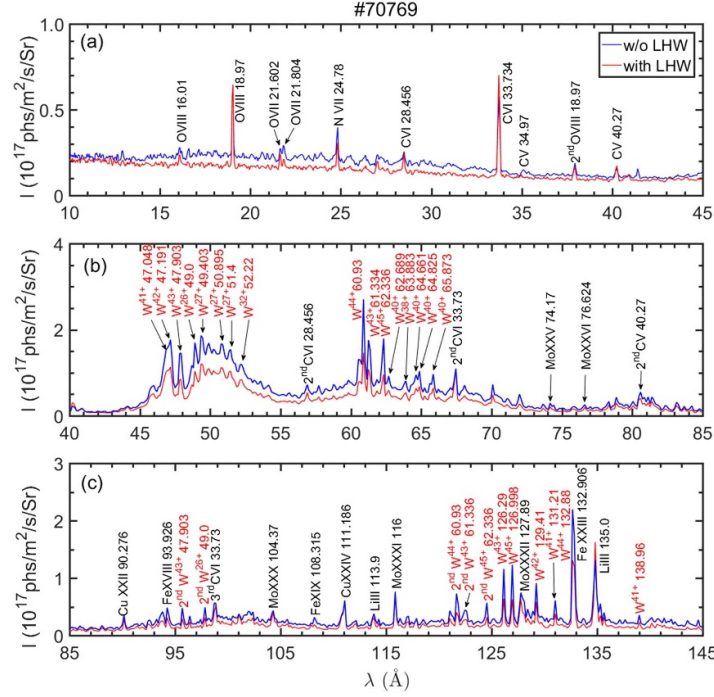
Figure 9. EUV spectra in wavelength ranges of (*a*) 10–45 Å, (*b*) 45–85 Å and (*c*) 85–145 Å observed during H-mode phase with (at $t = 4.8$ s) and without (at $t = 5.0$ s) LHW in #70769 discharge with $T_e \sim 2.6$ keV.
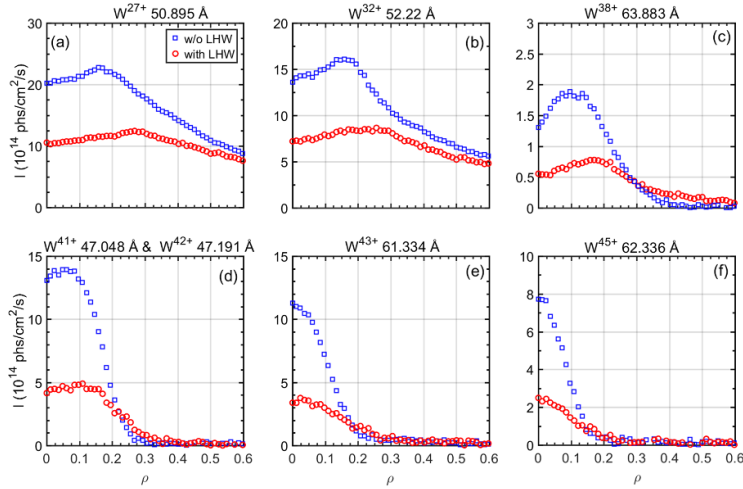

Figure 10. Radial intensity profiles of (*a*) W^{27+} at 50.895 Å, (*b*) W^{32+} at 52.22 Å, (*c*) W^{38+} at 63.883 Å, (*d*) W^{41+} at 47.048 Å and W^{42+} 47.191 Å, (*e*) W^{43+} at 61.334 Å and (*f*) W^{45+} at 62.336 Å during H-mode phase with (red circle) and without LHW (blue square) in #70769 discharge.

velocity, electron temperature and ion temperature on turbulent and neoclassical transports of the tungsten ion are studied. Figure 12 contrasts the radial profile of tungsten transport coefficients with and without LHW injection. As illustrated in figure 12(*a*), the diffusion of tungsten ions is predominantly driven by the turbulent diffusion due to the high ETG in the H-mode plasma. In the NBI phase without LHW, the neoclassical convection velocity dominates over the turbulent convection velocity, which is the primary reason for the tungsten accumulation. During the LHW phase, the outward turbulent diffusion of tungsten ions increases and the inward neoclassical convection decreases, leading to a significant reduction in the

tungsten content, as shown in figures 12(*a*) and (*b*). The ratio of total convection velocity to total diffusion coefficient can be replaced by the normalized density gradient of W ions as follows;

$$\frac{v}{D} = \frac{\nabla n_w}{n_w}. \tag{1}$$

In the presence of LHW power, the ratio of v/D increases and resultantly the peaked W density profile is smoother than the case of the absence of LHW power. However, experimental observations reveal that the LHW injection leads to changes
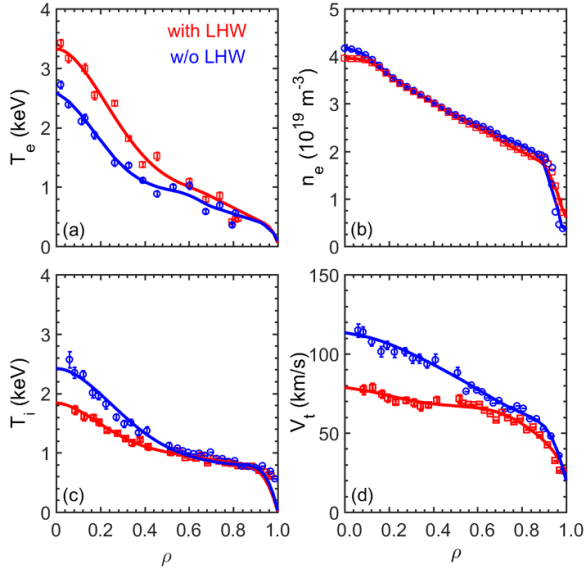
Figure 11. Comparisons of radial profiles of (*a*) electron temperature, T_e, and (*b*) electron density, n_e, (*c*) ion temperature, T_i, and (*d*) toroidal rotation velocity, V_t, with ($t = 4.8$ s) and without ($t = 5.0$ s) LHW in #70769 discharge.

in several plasma parameters, e.g. electron and ion temperatures and toroidal rotation. To investigate the effect of electron temperature (T_e), ion temperature (T_i) and rotation velocity (V_t) on the tungsten transport coefficients, firstly, the transport coefficients were calculated using the discharge without LHW. The result was set as the initial parameter group including T_e, V_t, T_i and n_e profiles in the discharge phase without LHW. To check the individual impact of T_e, T_i, and V_t in the discharge with LHW, the simulation was repeated in sequence by replacing each parameter in the initial parameter group with the same parameter in the discharge phase with LHW. For example, when T_e in the discharge phase with LHW is selected, all other parameters in the initial parameter group are unchanged in the simulation. The transport coefficients obtained from each simulation were then compared with those in the initial parameter group to examine the individual contribution of T_e, T_i and V_t. The impact of these parameters on the transport of tungsten ions is analyzed below.

4.1. Impact of electron temperature on tungsten transport

Effective suppress of the tungsten accumulation by ECRH has been proven due to favorite effects of increase in the ETG and enhancement of the turbulent diffusion [8]. Figure 13 presents the radial profiles of transport coefficients calculated for low (without LHW) and high (with LHW) electron temperatures. All other plasma parameters are used for the case without LHW. Similar to the effect of ECRH on tungsten transport, in the discharge #70769, the electron temperature is effectively increased by the LHW injection while forming a steeper temperature gradient, as shown in figure 13(*d*). Resultantly, it

leads to a significant enhancement of the turbulent diffusion of tungsten ions through the electron micro-instability mode like trapped electron mode (TEM) and ETG mode. Figures 14(*a*) and (*b*) illustrate the real frequency and linear net growth rate of the micro-instability mode at low and high electron temperatures. As the ETG increases, the growth rate at $k_y \rho_s > 1$ raises obviously, suggesting destabilization of the electron micro-instability mode. The increase in the ETG has a minor effect on the radial convection, and then this effect is negligible compared to the pronounced change in the turbulent diffusion.

4.2. Impact of toroidal rotation on tungsten transport

Acceleration of the toroidal rotation induced by the NBI injection is the primary reason for the tungsten accumulation. Experimental observations indicate a significant decrease in the toroidal rotation speed following the LHW injection. It demonstrates that the tungsten content can be controlled with the LHW by decelerating the toroidal rotation. Figure 15 contrasts the impact of the toroidal rotation induced by the LHW on tungsten impurity transport. Following a reduction of the toroidal rotation, the inward neoclassical convection of the tungsten ion notably diminishes by the LHW, and thereby the tungsten accumulation can be effectively controlled. The influence of the LHW on the toroidal rotation is frequently observed in EAST [50] even in discharges maintained with ion cyclotron range of heating (ICRF). However, there is no definitive physical model to clearly explain the underlying mechanism [51]. Only theoretical speculations exist, such as direct momentum input from the wave, edge shear flow [52], electron orbit loss [53] and trapped electron pinch effect [54].

4.3. Impact of ion temperature on tungsten transport

In #70769 and #80672 discharges, the ion temperature significantly decreased during the LHW phase. This phenomenon has been also observed in the HL-2A tokamak. The reason is considered to be related to the edge shear flow (E_r) [52]. The normalized logarithmic gradient of the ion temperature is compared between two cases with and without LHW injection in figure 16(*d*). Decrease in the ITG significantly enhances the inward neoclassical convection, while it simultaneously reduces the turbulent diffusion by stabilizing the ITG mode. AS a result, the inward transport of tungsten ions is enhanced, as illustrated in figures 16(*a*)–(*c*). As calculated with TGLF, the linear growth rate of the ion micro-instability mode significantly decreases with less ITGs, as shown in figure 14(*d*). A steep ITG truly contributes to the expulsion of impurity ions [55, 56]. Despite this, the significant reduction in the tungsten content following the LHW injection indicates that unfavorable effect on the tungsten accumulation suppression originated from the decrease in the ITG is fully compensated by favorable effects originated from the decrease in the toroidal rotation and the increase in the electron temperature.
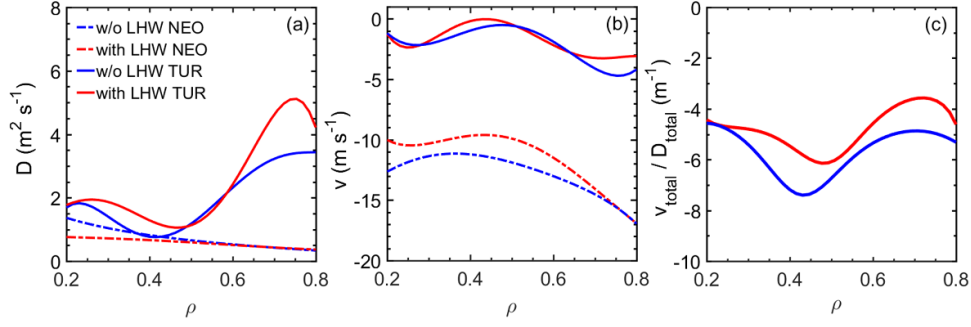
Figure 12. Radial profiles of (*a*) diffusion coefficient, *D*, (*b*) convection velocity, *v*, and (*c*) ratio of total convection velocity to total diffusion coefficient for tungsten ions with (red) and without (blue) LHW. Solid and dot lines denote turbulent and neoclassical terms, respectively. The 'total' means the sum of neoclassical and turbulent contributions.
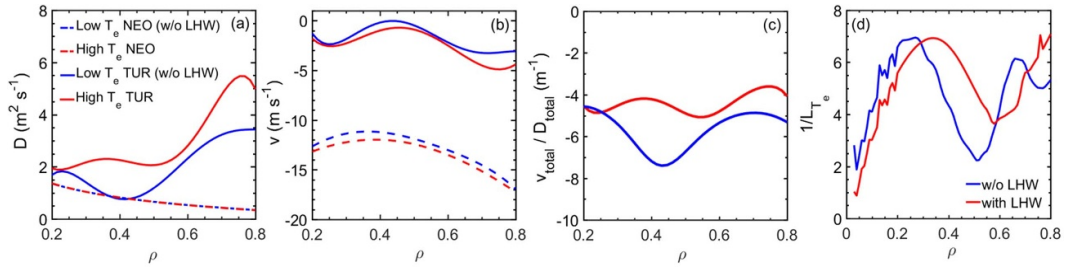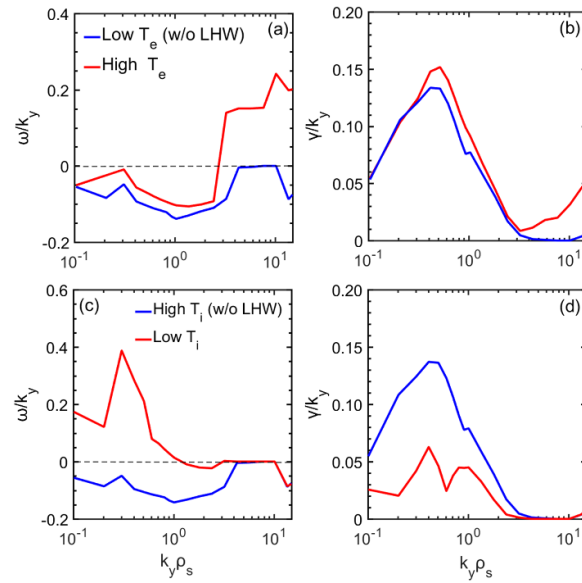

Figure 13. Radial profiles of (*a*) diffusion coefficient, *D*, (*b*) convection velocity, *v*, and (*c*) ratio of total convection velocity to total diffusion coefficient of tungsten ions at high (red) and low (blue) electron temperatures, and radial profiles of (*d*) normalized logarithmic gradients of electron temperature in the case with (red) and without (blue) LHW. The 'total' means the sum of neoclassical and turbulent contributions. Transport coefficients were calculated for low (without LHW) and high (with LHW) electron temperatures. All other plasma parameters are used for the case without LHW.

Figure 14. (*a*) Micro-instability mode frequencies and (*b*) growth rate at low (blue) and high (red) electron temperatures and (*c*) micro-instability mode frequencies and (*d*) growth rate at low (blue) and high (red) ion temperatures. The parameter of γ means linear growth rate. The mode frequency and growth rate are obtained by TGLF code based on the electron and ion temperature radial gradients at $\rho \sim 0.5$. When the mode frequency ranges at $\omega > 0$, the electron micro-instability mode becomes dominant.
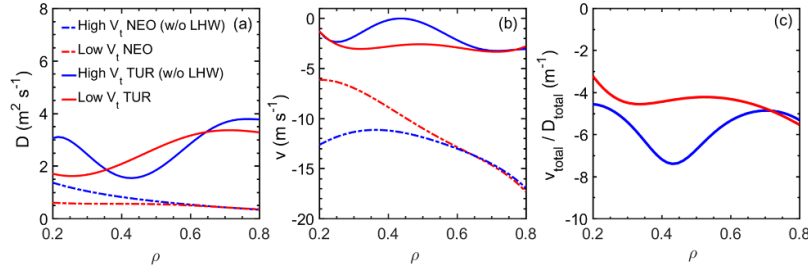
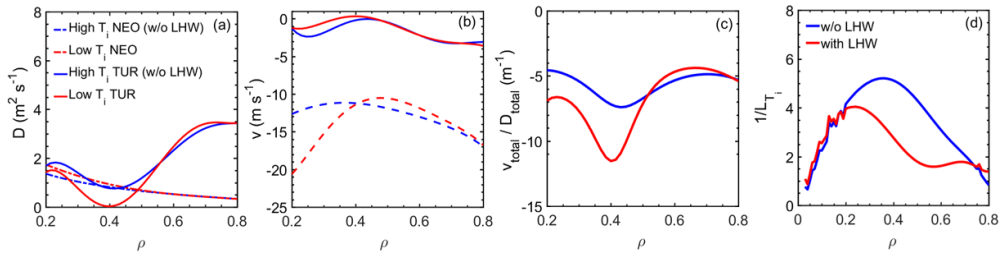**Figure 15.** Radial profiles of (*a*) diffusion coefficients, *D*, (*b*) convection velocities, *v*, and (*c*) ratio of total convection velocity to total diffusion coefficient of tungsten ions at low (red) and high (blue) ion temperatures, and radial profiles of (*d*) normalized logarithmic radial gradients of ion temperature with (red) and without (blue) LHW. Neoclassical (dashed lines) and turbulent (solid lines) transport coefficients are calculated for high (without LHW) and low (with LHW) ion temperatures. All other plasma parameters are used for the case without LHW.

Figure 16. Radial profiles of (*a*) diffusion coefficients, *D*, (*b*) convection velocities, *v*, and (*c*) ratio of total convection velocity to total diffusion coefficient of tungsten ions at low (red) and high (blue) ion temperatures, and radial profiles of (*d*) normalized logarithmic radial gradients of ion temperature with (red) and without (blue) LHW. Neoclassical (dashed lines) and turbulent (solid lines) transport coefficients are calculated for high (without LHW) and low (with LHW) ion temperatures. All other plasma parameters are used for the case without LHW.

4.4. Comparison of tungsten densities under different plasma parameters

Based on the calculation by the STRAHL impurity transport code, in which the transport coefficients are used those calculated by TGYRO as the input parameter, the impact of transport modifications caused by variations in T_e, T_i, and V_t are evaluated on the density profile of tungsten ions. The result is shown in figure 17. Compared to the tungsten ion density in the case without LHW, the tungsten density in the plasma core decreases from 3.69×10^{15} m^{-3} to 1.98×10^{15} m^{-3} during the LHW phase. The reduction of approximately 46% in the calculation is consistent with the experimental result of 45% reduction, as shown in table 2. The high ETG and low toroidal rotation velocity reduce the tungsten density to 1.46×10^{15} m^{-3} and 2.58×10^{15} m^{-3}, respectively. This indicates that higher ETG has more favorite effect on the tungsten control compared to the reduction in the toroidal rotation. Lower ITG leads to the density buildup of the tungsten ion to 5.63×10^{15} m^{-3} (see figure 17(*a*)). However, decrease in the toroidal rotation and increase in the ETG have a sufficient tungsten control effect by offsetting the unfavorable effect of the reduced ITG, and thus it leads to a significant decrease in the tungsten density.

5. Discussions

In #80672 and #70769 discharges, following the injection of the LHW, the ELM frequency increased from 75 Hz to 100 Hz and from 120 Hz to 180 Hz, respectively. The move to higher ELM frequencies is basically favorable for expelling the impurity ions from the pedestal region [57, 58]. Therefore, the impurity ions staying in the plasma edge should be more affected by the ELMs. However, the experimental observations shows that the reduction of impurity ions in relatively lower ionization stages staying near the plasma edge, e.g. Fe^{17+} and Mo^{24+} ions, is not so sufficient during the LHW phase compared with impurity ions in higher ionization stages locating in the plasma core, e.g. Fe^{22+} and Mo^{30+} ions, as illustrated in figure 5. Moreover, as shown in figure 9, after the LHW injection, the line emission intensities of molybdenum and iron ions exhibited no significant changes compared to those of tungsten ions. This implies that the increase in the ELM frequency during the LHW phase for both experiments did not significantly enhance the impurity flushing out, and thus the impact of the increased ELM frequency on tungsten impurity transport was negligibly small in the present study. Moreover, high frequency ELM can even lead to the enhancement of impurity sources [59], which may explain the observed increase in the tungsten impurity source in the experiment. The increase in the tungsten impurity source induced by a plasma-wall interaction during the LHW phase and the reduction of the ITG, which can enhance the neoclassical inward convection and decrease the turbulent diffusion, are fully counterbalanced by changes in the electron temperature and toroidal rotation. These changes also lead to the mitigation of the tungsten accumulation caused by the NBI heating.
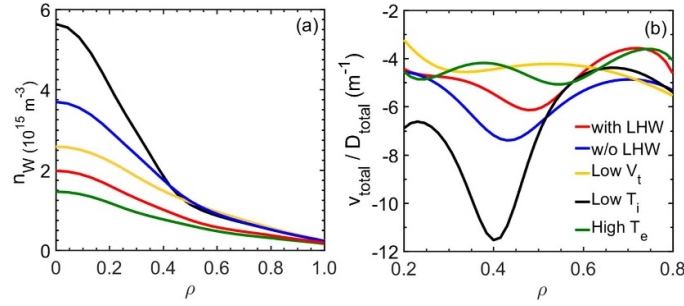
Figure 17. (*a*) Radial profile of total tungsten density calculated by STRAHL code based on the transport coefficients in cases of with LHW (red), without LHW (blue), low toroidal rotation velocity (yellow), high electron temperature (green) and low ion temperature (black) and (*b*) radial profiles of ratios of total convection velocity to total diffusion coefficient. The calculation is performed for the case of high T_e, low T_i and low V_t based on the transport coefficient from figures 13, 15 and 16.

Table 2. Tungsten densities calculated by STRAHL code in a variety of parameters.

	Tungsten density (m^{-3})	Percentage change[a]
w/o LHW	3.69×10^{15}	—
with LHW	1.98×10^{15}	-46%
Low V_t	2.58×10^{15}	-30%
Low T_i	5.63×10^{15}	$+53\%$
High T_e	1.46×10^{15}	-60%

[a] Comparison to the case without LHW. Negative/positive values indicate decrease/increase in the tungsten density, respectively.

In #80672 discharge, the LHW injection did not make a significant increase in the electron temperature, which might be attributable to the edge deposition of LHW power due to the low toroidal magnetic field ($B_T = 1.67$ T) and the relatively low electron density ($n_{e0} = 3.0 \times 10^{19}$ m^{-3}). Nonetheless, the LHW injection suppressed the tungsten accumulation by reducing the toroidal rotation velocity in the NBI-heated plasma. Changes in the plasma toroidal rotation induced by the LHW have been observed in several tokamaks, such as Alcator C-Mod [51, 60, 61], HL-2A [52], JET [62], Tore Supra [63] and EAST [22, 50, 64]. However, the physical mechanism why the LHW can change the toroidal rotation still remains unclear, while several physical models have been proposed to explain it [51], e.g. direct momentum input from LHW, electron orbit loss, pinch effect of trapped electrons and radial drift of LHW resonant electrons.

6. Conclusions

After the LHW injection in the low q_{95} plasma with NBI heating, 70% reduction in the tungsten concentration, C_W ($=n_W/n_e$), from 2.0×10^{-5} to 6×10^{-6} was observed with decrease in the toroidal rotation velocity from 110 km s^{-1} to 70 km s^{-1}. Similar result was also observed in the high q_{95} plasma. In this experiment, the LHW was injected intermittently with a 50% duty cycle and a frequency of 3 Hz. Periodic variations with the LHW injection were clearly identified in

the electron temperature, toroidal rotation and tungsten concentration. During the LHW phase, the tungsten concentration decreased by approximately 45%, from 9.5×10^{-5} to 5.3×10^{-5}, and the radial profile of tungsten ions flattened with shifting the peak position outward. Significant changes are found in the tungsten transport.

The tungsten transport coefficient is modeled using the TGYRO simulation code based on the radial profile analysis in discharge #70769. The simulation results indicate that the tungsten impurity transport is mainly dominated by the turbulent diffusion and neoclassical convection. During the LHW phase, the turbulent diffusion of tungsten ions is enhanced and the neoclassical convection is weakened. By comparing the transport coefficient of tungsten ions among different toroidal rotation velocities and electron temperatures, it is found that lower toroidal rotation velocities weaken the inward neoclassical convection, while higher electron temperatures enhance the outward turbulent diffusion. Although the turbulence measurement is poor in the present experiment, the simulation suggests that the growth rate of electron micro-instability modes increases during the LHW phase. Thus, the additional heating by LHW can suppress the tungsten accumulation in NBI-heated plasmas based on the following two aspects;

1. The LHW heating decreases the plasma toroidal rotation velocity. It leads to the reduction of the inward neoclassical convection of tungsten ions.
2. Increase in the ETG enhances the turbulent diffusion of tungsten ions through a destabilization of electron turbulent instability modes.

Nevertheless, the physical mechanism to explain the relation between the LHW and toroidal rotation still remains unclear. In the future EAST experiment various experimental scenarios are being planned to explore the relation between the LHW and the toroidal rotation. Experimental studies in EAST tokamak aimed at preventing the tungsten accumulation induced by NBI heating will provide an important reference

for the operation of ITER and the design of future fusion reactors.

ORCID iDs

Yunxin Cheng ⬤ https://orcid.org/0000-0002-9195-2757
Chengxi Zhou ⬤ https://orcid.org/0000-0001-9200-1665
Xiang Gao ⬤ https://orcid.org/0000-0003-1885-2538
Shouxin Wang ⬤ https://orcid.org/0000-0001-9600-4038
Wenmin Zhang ⬤ https://orcid.org/0009-0000-9980-6765
Zhen Zhou ⬤ https://orcid.org/0009-0000-8261-7837
Liqing Xu ⬤ https://orcid.org/0009-0003-7340-1083
Yingying Li ⬤ https://orcid.org/0000-0002-2978-908X
Miaohui Li ⬤ https://orcid.org/0000-0002-3658-8243
Darío Mitnik ⬤ https://orcid.org/0000-0003-0193-0958
Haiqing Liu ⬤ https://orcid.org/0000-0001-6892-358X
Guosheng Xu ⬤ https://orcid.org/0000-0001-8495-8678

References

[1] Philipps V. 2011 *J. Nucl. Mater.* **415** S2–S9
[2] Wan Y.X. *et al* 2017 *Nucl. Fusion* **57** 102009
[3] Odstrcil T., Pütterich T., Angioni C., Bilato R., Gude A. and Odstrcil M. 2018 *Plasma Phys. Control. Fusion* **60** 014003
[4] Hoshino K., Toma M., Shimizu K., Nakano T., Hatayama A. and Takizuka T. 2011 *Nucl. Fusion* **51** 083027
[5] Köchl F. *et al* 2018 *Plasma Phys. Control. Fusion* **60** 074008
[6] Angioni C. *et al* 2014 *Nucl. Fusion* **54** 083028
[7] Angioni C., Sertoli M., Bilato R., Bobkov V., Loarte A., Ochoukov R., Odstrcil T., Pütterich T. and Stober J. 2017 *Nucl. Fusion* **57** 056015
[8] Shi S.Y. *et al* 2022 *Nucl. Fusion* **62** 066031
[9] Angioni C., Casson F.J., Mantica P., Pütterich T., Valisa M., Belli E.A., Bilato R., Giroud C. and Helander P. 2015 *Phys. Plasmas* **22** 055902
[10] Lerche E. *et al* 2016 *Nucl. Fusion* **56** 036022
[11] Urbanczyk G., Zhang X.J., Colas L., Ekedahl A., Heuraux S., Li J.G., Qin C.M., Zhao Y.P., Zhang L. and Yang X.D. 2018 *Nucl. Mater. Energy* **17** 274–8
[12] Song Y.T. *et al* 2022 *IEEE Trans. Plasma Sci.* **50** 4330
[13] Gong X.Z. *et al* 2024 *Nucl. Fusion* **64** 112013
[14] Zhang L. *et al* 2017 *Annual Meeting of the APS Division of Plasma Physics* (*Milwaukee, Wisconsin*) *23–27 October 2017* vol 62 (available at: https://meetings.aps.org/Meeting/DPP17/Session/TO4.10)
[15] Xu Z. *et al* 2021 *Chin. Phys. B* **30** 075205
[16] Zhang L. *et al* 2017 *Nucl. Mater. Energy* **12** 774–8
[17] Wan B.N. *et al* 2022 *Nucl. Fusion* **62** 042010
[18] Li Y.L. *et al* 2018 *Phys. Plasmas* **25** 082503
[19] Guo Z.X. *et al* 2024 *Nucl. Fusion* **64** 076026
[20] Hu C.D. *et al* 2015 *Plasma Sci. Technol.* **17** 817
[21] Xu W.Y., Xu H., Wu D., Yang Y., Zhang J., Wang X., Wang J., Hou Y., Zhang L. and Li M. 2024 *IEEE Trans. Plasma Sci.* **52** 5159–72
[22] Liu F.K. *et al* 2015 *Nucl. Fusion* **55** 123022
[23] Xu Z. *et al* 2021 *Nucl. Instrum. Methods A* **1010** 165545
[24] Zhang L. *et al* 2015 *Rev. Sci. Instrum.* **86** 123509
[25] Zhang L. *et al* 2019 *Nucl. Instrum. Methods A* **916** 169–78
[26] Li L. *et al* 2021 *Plasma Sci. Technol.* **23** 075102
[27] Zhang W.M. *et al* 2022 *Phys. Scr.* **97** 045604
[28] Zhang W.M. *et al* 2024 *Phys. Scr.* **99** 105609
[29] Cheng Y.X. *et al* 2022 *IEEE Trans. Plasma Sci.* **50** 691–9
[30] Qing Z.L., Junyu Z., Li Y., Qingsheng H., Yanqing J., Tao Z., Xiaoqi X., Bhatti S.H. and Xiang G. 2010 *Plasma Sci. Technol.* **12** 144–8
[31] Zhao H., Zhou T., Liu Y., Ti A., Ling B., Austin M.E., Houshmandyar S., Huang H., Rowan W.L. and Hu L. 2018 *Rev. Sci. Instrum.* **89** 10H111
[32] Liu H.Q. *et al* 2016 *J. Instrum.* **11** C01049
[33] Zhang S.B., Gao X., Ling B., Wang Y., Zhang T., Han X., Liu Z., Bu J. and Li J. 2014 *Plasma Sci. Technol.* **16** 311
[34] Mao H.M. *et al* 2017 *Rev. Sci. Instrum.* **88** 043502
[35] Duan Y.M., Hu L.Q., Mao S.T., Chen K.Y. and Lin S.Y. 2012 *Rev. Sci. Instrum.* **83** 093501
[36] Candy J., Holland C., Waltz R.E., Fahey M.R. and Belli E. 2009 *Phys. Plasmas* **16** 060704
[37] Belli E.A. and Candy J. 2008 *Plasma Phys. Control. Fusion* **50** 095010
[38] Belli E.A. and Candy J. 2011 *Plasma Phys. Control. Fusion* **54** 015015
[39] Staebler G.M., Kinsey J.E. and Waltz R.E. 2005 *Phys. Plasmas* **12** 102508
[40] Kinsey J.E., Staebler G.M. and Waltz R.E. 2008 *Phys. Plasmas* **15** 055908
[41] Staebler G.M., Howard N.T., Candy J. and Holland C. 2017 *Nucl. Fusion* **57** 066046
[42] Dux R. 2004 Report IPP 10/27 (Max-Planck-Institut für Plasmaphysik) (available at: https://hdl.handle.net/11858/11800-11001M-10000-10027-12036-E)
[43] Zuo G.Z., Hu J.S., Li J.G., Sun Z., Mansfield D.K. and Zakharov L.E. 2013 *J. Nucl. Mater.* **438** S90–S95
[44] Xu W. *et al* 2018 *Fusion Eng. Des.* **137** 202–8
[45] Günter S., Gude A., Lackner K., Maraschek M., Pinches S., Sesnic S. and Wolf R. (ASDEX Upgrade Team) 1999 *Nucl. Fusion* **39** 1535
[46] Nave M.F.F. *et al* 2003 *Nucl. Fusion* **43** 1204–13
[47] Qiang X., Xiang G., Yinxian J., Haiqing L., Nan S., Yongfei C. and Xingde T. 2008 *Plasma Sci. Technol.* **10** 519
[48] Li Y.Y. *et al* 2014 *Rev. Sci. Instrum.* **85** 11E428
[49] Shi S.Y. *et al* 2022 *Nucl. Fusion* **62** 066032
[50] Yin X.-H. *et al* 2017 *Chin. Phys. B* **26** 115203
[51] Rice J.E. *et al* 2013 *Nucl. Fusion* **53** 093015
[52] Xiao G.L. *et al* 2017 *Phys. Plasmas* **24** 122507
[53] Sakamoto Y., Ide S., Yoshida M., Koide Y., Fujita T., Takenaga H. and Kamada Y. 2006 *Plasma Phys. Control. Fusion* **48** A63
[54] Gao Z., Fisch N.J. and Qin H. 2011 *Phys. Plasmas* **18** 082507

[55] Han M.K. *et al* 2021 *Nucl. Fusion* **61** 046010
[56] Sudo S. 2016 *Plasma Phys. Control. Fusion* **58** 043001
[57] Kallenbach A. *et al* 2009 *Nucl. Fusion* **49** 045007
[58] Wade M.R., Burrell K.H., Leonard A.W., Osborne T.H. and Snyder P.B. 2005 *Phys. Rev. Lett.* **94** 225001
[59] Huber A. *et al* 2020 *Nucl. Mater. Energy* **25** 100859
[60] Ince-Cushman A. *et al* 2009 *Phys. Rev. Lett.* **102** 035002
[61] Rice J.E. *et al* 2009 *Nucl. Fusion* **49** 025004
[62] Eriksson L.-G., Hellsten T., Nave M.F.F., Brzozowski J., Holmström K., Johnson T., Ongena J. and Zastrow K.-D. 2009 *Plasma Phys. Control. Fusion* **51** 044008
[63] Chouli B. *et al* 2015 *Plasma Phys. Control. Fusion* **57** 125007
[64] Shi Y.J. *et al* 2011 *Phys. Rev. Lett.* **106** 235001